

Contactless Electromagnetic Phase-Shift Flowmeter for Liquid Metals

Jānis Priede¹, Dominique Buchenau² and Gunter Gerbeth²

¹Applied Mathematics Research Centre, Coventry University, United Kingdom

²Forschungszentrum Dresden-Rossendorf, MHD Department, Germany

E-mail: j.priede@coventry.ac.uk

Abstract. We present a concept and test results of an eddy-current flowmeter for liquid metals. The flow rate is determined by applying a weak ac magnetic field to a liquid metal flow and measuring the flow-induced phase disturbance in the external electromagnetic field. The phase disturbance is found to be more robust than that of the amplitude used in conventional eddy-current flowmeters. The basic characteristics of this type of flowmeter are analysed using simple theoretical models, where the flow is approximated by a solid body motion. Design of such a flowmeter is presented and its test results reported.

Keywords: Electromagnetic flowmeter, liquid metal, ac magnetic field

PACS numbers: 41.20.Gz, 47.60.Dx, 47.65.-d, 47.80.Cb

Submitted to: *Meas. Sci. Technol.*

1. Introduction

Accurate and reliable flow rate measurements are required in many technological processes using liquid metals. Commercially available electromagnetic flowmeters typically use electrodes in direct contact to the liquid to measure the voltage induced by the flow in dc magnetic field [1, 2, 3, 4]. The use of electrodes is problematic in aggressive media like molten metals, for which a contactless treatment is preferable [5]. A well-known example of such a contactless flowmeter is the magnetic flywheel, which is described in the textbook of Shercliff [1] and employed by Bucenieks [6, 7] for the flow rate measurements. Such kind of flowmeters have recently been reembodied under the name of Lorentz force velocimetry [8, 9]. As the name suggests, the Lorentz force sensors measure the electromagnetic force exerted by the flow on a closely placed permanent magnet. This force is proportional to the product of the electrical conductivity of the fluid and the square of the applied magnetic field strength. Another type of flowmeter using a single rotating magnet has recently been reported in [10, 11]. This sensor is based on the equilibrium of the electromagnetic torques caused by the flow on the magnet and by the magnet on the flow. The equilibrium rotation rate is, in a reasonable range of parameters, independent of both the strength of the permanent magnet and the conductivity of the liquid, which makes the measurements insensitive to temperature variations in the liquid.

Alternatively, the flow of liquid metal can be determined in a contactless way by eddy-current flowmeters, which measure the flow-induced perturbation of an externally applied magnetic field [12, 13]. This principle underlies also the so-called flow tomography approach using either dc [14] or ac magnetic fields [15]. The main problem of this method is to measure a weak induced magnetic field with the relative amplitude of the order of magnitude of the magnetic Reynolds number $Rm \sim 10^{-4} - 10^{-1}$ on the background of the applied magnetic field. There are a number of measurement schemes known which rely on the geometrical compensation of the applied field by a proper arrangement of sending and receiving coils so that only the signal induced by the flow is measured [16, 17]. Such flowmeters employ the flow-induced asymmetry of the magnetic field. Unfortunately, there are a number of side effects such as, for example, the thermal expansion, which can also cause some asymmetry between the receiving coils.

As the flow can disturb not only the amplitude of an ac magnetic field but also its phase distribution, the latter can also be used for the flow rate measurements [18, 19]. In this paper, we analyse the basic characteristics of such a phase-shift flowmeter, present its technical implementation and report the test results.

The paper is organised as follows. The basic physical effects are considered in Section 2 using a simple model where the liquid flow is approximated by a solid body motion. In Section 3 we describe the realization of the phase-shift sensor and present flow rate measurements at two different liquid metal loops. The paper is concluded by a summary in Section 4.

2. Mathematical model

2.1. Basic equations

Consider a medium of electrical conductivity σ moving with the velocity $\mathbf{v} = \mathbf{e}_x V$ in an ac magnetic field with the induction \mathbf{B} alternating harmonically with the angular frequency ω . The induced electric field follows from the Maxwell-Faraday equation as $\mathbf{E} = -\nabla\Phi - \partial_t \mathbf{A}$, where Φ is the electric potential, \mathbf{A} is the vector potential and $\mathbf{B} = \nabla \times \mathbf{A}$. The density of the electric current induced in the moving medium is given by Ohm's law

$$\mathbf{j} = \sigma(\mathbf{E} + \mathbf{v} \times \mathbf{B}) = \sigma(-\nabla\Phi - \partial_t \mathbf{A} + \mathbf{v} \times \nabla \times \mathbf{A}).$$

Assuming the ac frequency to be sufficiently low to neglect the displacement current, Ampere's law $\mathbf{j} = \frac{1}{\mu_0} \nabla \times \mathbf{B}$ leads to the following advection-diffusion equation for the vector potential

$$\partial_t \mathbf{A} + (\mathbf{v} \cdot \nabla) \mathbf{A} = \frac{1}{\mu_0 \sigma} \nabla^2 \mathbf{A}, \quad (1)$$

where the gauge invariance of \mathbf{A} has been used to specify the scalar potential as

$$\Phi = \mathbf{v} \cdot \mathbf{A} - \frac{1}{\mu_0 \sigma} \nabla \cdot \mathbf{A}.$$

In the following, we consider an applied magnetic field varying in time harmonically as $\mathbf{A}_0(\mathbf{r}, t) = \mathbf{A}_0(\mathbf{r}) \cos(\omega t)$, which allows us to search for a solution in the complex form $\mathbf{A}(\mathbf{r}, t) = \Re[\mathbf{A}(\mathbf{r}) e^{i\omega t}]$. Then equation (1) for the amplitude distribution of the vector potential takes the form

$$i\omega \mathbf{A} + (\mathbf{v} \cdot \nabla) \mathbf{A} = \frac{1}{\mu_0 \sigma} \nabla^2 \mathbf{A}. \quad (2)$$

Further we focus on a simple 2D externally applied magnetic field, which is invariant along the unit vector $\boldsymbol{\epsilon}$. Such a magnetic field can be specified by a single component of the vector potential $\mathbf{A} = \boldsymbol{\epsilon} A$ as $\mathbf{B} = \nabla \times \boldsymbol{\epsilon} A = -\boldsymbol{\epsilon} \times \nabla A$, where \mathbf{B} has only two components in the plane perpendicular to $\boldsymbol{\epsilon}$. The continuity of \mathbf{B} at the interface S between conducting and insulating media imply the following boundary conditions:

$$[A]_S = [\partial_n A]_S = 0, \quad (3)$$

where $[f]_S$ denotes the jump of quantity f across the boundary S ; $\partial_n \equiv (\mathbf{n} \cdot \nabla)$ is the derivative normal to the boundary.

2.2. Solution for a single harmonic of the magnetic field

We start with a simple model shown in figure 1(a), where the conducting medium is a layer of thickness $2H$, and the applied magnetic field is a harmonic standing wave with the vector potential amplitude given by

$$\mathbf{A}_0(\mathbf{r}, t) = \mathbf{e}_z A_0(\mathbf{r}, t) = \mathbf{e}_z \hat{A}_0(y) \cos(kx) \cos(\omega t),$$

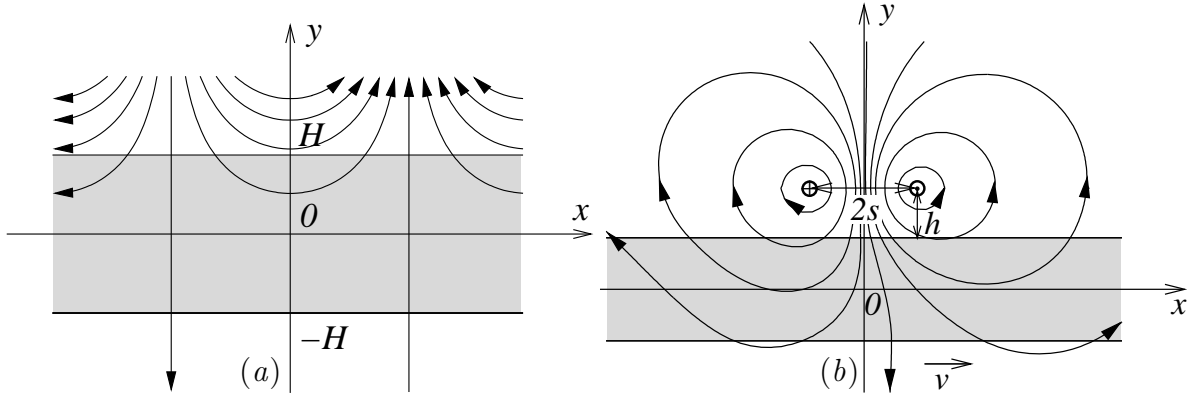


Figure 1. Model of a conducting layer of thickness $2H$ in an external magnetic field represented by a standing harmonic wave (a) and generated by a couple of straight wires (b).

where k is the wavenumber in the x -direction. Henceforth, we choose the half-thickness H as the length scale and introduce a dimensionless ac frequency and the magnetic Reynolds number,

$$\bar{\omega} = \mu_0 \sigma \omega H^2, \quad (4)$$

$$Rm = \mu_0 \sigma V H, \quad (5)$$

where the latter represents a dimensionless velocity. It is important to note that this key parameter depends on the product of the physical velocity and electrical conductivity. Although for a typical liquid metal flow $Rm \ll 1$, the following analysis will not be restricted to this case unless stated otherwise. For a free space, where $\sigma = 0$, equation (2) takes the form

$$\frac{d^2 \hat{A}_0}{dy^2} - k^2 \hat{A}_0 = 0, \quad (6)$$

and has the solution

$$\hat{A}_0(y; k) = C_0 e^{|k|(y-1)}, \quad (7)$$

where the constant

$$C_0 = \hat{A}_0(1; k) \quad (8)$$

defines the amplitude of the Fourier mode with the wavenumber k of the external magnetic field at the upper boundary of the layer. It is important to note that the external magnetic field, which is assumed in the form of a standing wave, can be represented as a superposition of two oppositely travelling waves

$$A_0(\mathbf{r}, t) = \frac{1}{2} [A_0^+(\mathbf{r}, t) + A_0^-(\mathbf{r}, t)],$$

where $A_0^\pm(\mathbf{r}, t) = \hat{A}_0(y) \cos(\omega t \pm kx)$. This implies that the solution can be sought in a similar form as

$$A(\mathbf{r}, t) = \frac{1}{2} [A^+(\mathbf{r}, t) + A^-(\mathbf{r}, t)],$$

where $A^\pm(\mathbf{r}, t) = \Re[\hat{A}(y; \pm k)e^{i(\omega t \pm kx)}]$ are oppositely travelling fields. The solution governed by equation (6) in the free space above the layer ($y \geq 1$), can be written as

$$\hat{A}(y; k) = \hat{A}_0(y; k) + \hat{A}_1(y; k), \quad (9)$$

where the first term represents the external field (7) and $\hat{A}_1(y; k) = C_1 e^{-|k|(y-1)}$ is the induced field. In the free space below the layer, $y \leq -1$, the solution satisfying (6) is

$$\hat{A}(y; k) = C_3 e^{|k|(y+1)}. \quad (10)$$

In the conducting layer, $-1 \leq y \leq 1$, equation (2) for a travelling field takes the form

$$\frac{d^2 \hat{A}}{dy^2} - \kappa^2 \hat{A} = 0, \quad (11)$$

where $\kappa(k) = \sqrt{k^2 + i(\bar{\omega} + kRm)}$, and has the solution

$$\hat{A}(y; k) = C_2 \sinh(\kappa y) + D_2 \cosh(\kappa y). \quad (12)$$

The unknown constants, which are regarded as functions of the wavenumber k , are found from the boundary conditions (3) as follows

$$C_2 = C_0 |k| / (|k| \sinh(\kappa) + \kappa \cosh(\kappa)) \quad (13)$$

$$D_2 = C_0 |k| / (|k| \cosh(\kappa) + \kappa \sinh(\kappa)), \quad (14)$$

$$C_1 = D_2 \cosh(\kappa) + C_2 \sinh(\kappa) - C_0, \quad (15)$$

$$C_3 = D_2 \cosh(\kappa) - C_2 \sinh(\kappa). \quad (16)$$

2.3. Solution for an external magnetic field generated by a couple of straight wires

The solution above can easily be extended to an external magnetic field generated by a finite-size coil. The simplest model of such a coil consists of two parallel straight wires fed with an ac current of amplitude I_0 flowing in the opposite directions along the z -axis at distance $2s$ in the x -direction and placed at height h above the upper surface of the layer, as shown in figure 1(b). The free-space distribution of the vector potential amplitude having only the z -component, which is further scaled by $\mu_0 I_0$, is governed by

$$\nabla^2 A_0 = -\delta(\mathbf{r} - h\mathbf{e}_y - s\mathbf{e}_x) + \delta(\mathbf{r} - h\mathbf{e}_y + s\mathbf{e}_x), \quad (17)$$

where $\delta(\mathbf{r})$ is the Dirac delta function and \mathbf{r} is the radius vector. The problem is solved by the Fourier transform $\hat{A}(y; k) = \int_{-\infty}^{\infty} A(x, y) e^{ikx} dx$, which converts (17) into

$$\frac{d^2 \hat{A}_0}{dy^2} - k^2 \hat{A}_0 = -f(k) \delta(y - h), \quad (18)$$

where $f(k) = \int_{-\infty}^{\infty} [\delta(x - s) - \delta(x + s)] e^{ikx} dx = 2i \sin(ks)$. The solution of (18) decaying at $y \rightarrow \pm\infty$ can be written as

$$\hat{A}_0(y; k) = c(k) e^{-|k|(y-h)}, \quad (19)$$

where the unknown coefficient

$$c(k) = \frac{f(k)}{2|k|} = \frac{i \sin(ks)}{|k|}. \quad (20)$$

follows from the boundary condition $\left[\frac{d\hat{A}}{dy} \right]_{y=h} = -f(k)$, which is obtained by integrating equation (18) over the singularity at $z = h$. The solution for a separate Fourier mode in the regions above, below and inside the layer is given, respectively, by expressions (9, 10) and (12) with the coefficients (13)–(16) containing the constant C_0 , which is defined by substituting (19) into (8). Then the spatial distribution of the complex vector potential amplitude is given by the sum of Fourier modes, which is defined by the inverse Fourier transform $A(x, y) = \frac{1}{2\pi} \int_{-\infty}^{\infty} \hat{A}(y; k) e^{-ikx} dk$ and can efficiently be calculated using the Fast Fourier Transform.

2.4. Numerical results

For physical interpretation of the following results, note that the magnetic flux through a surface is given by the circulation of the vector potential along the contour encircling that surface. For the simple 2D case under consideration, when the vector potential has only one component, the difference of the vector potential between two points defines the linear flux density between two lines parallel to the vector potential at those two points. The same holds also for the time derivative of the corresponding quantities. Thus, the difference of the vector potential amplitudes between two points is proportional to the e.m.f. amplitude which could be measured by an idealised coil consisting of two straight parallel wires placed along the z -axis at those points. Correspondingly, the single-point vector potential considered below gives the e.m.f. measured by a ‘wide’ coil with the second wire placed sufficiently far away in the region of a negligible magnetic field.

2.4.1. Single harmonic of the magnetic field The flux lines and the corresponding phase distribution of the vector potential are plotted in figure 2 for the layer at rest (a, c, e) and moving to the right with $Rm = 1$ (b, d, f). The flux components in the phase and shifted by $\pi/2$ relative to the applied magnetic field correspond to the time instants when the applied field is at maximum and absent, respectively. In the latter case, the magnetic field is entirely due to the eddy currents. Figure 2(e) shows that for the layer at rest, the phase is constant over a half-wavelength of the applied field and varies only with the vertical position except below the layer, where the phase does not vary at all. It is important to note that this phase distribution is actually piece-wise constant with the phase jumping by π across nodes of the standing wave. This phase discontinuity, which is crucial for the subsequent analysis, is caused by two adjacent halves of standing wave oscillating in opposite phases. As seen in figure 2(f), this simple phase distribution breaks down as soon as the layer starts to move. Although for a moving layer the phase is no longer horizontally constant, it is still vertically constant below the layer, where the field itself decays exponentially with the vertical distance. This is an important result, which illustrates why the phase measurements, in contrast to those of the amplitude, are more robust and, in this case, actually independent of the vertical position of the receiving coils. Note that such a perfect vertical phase homogeneity holds only when the applied magnetic field is a standing harmonic wave.

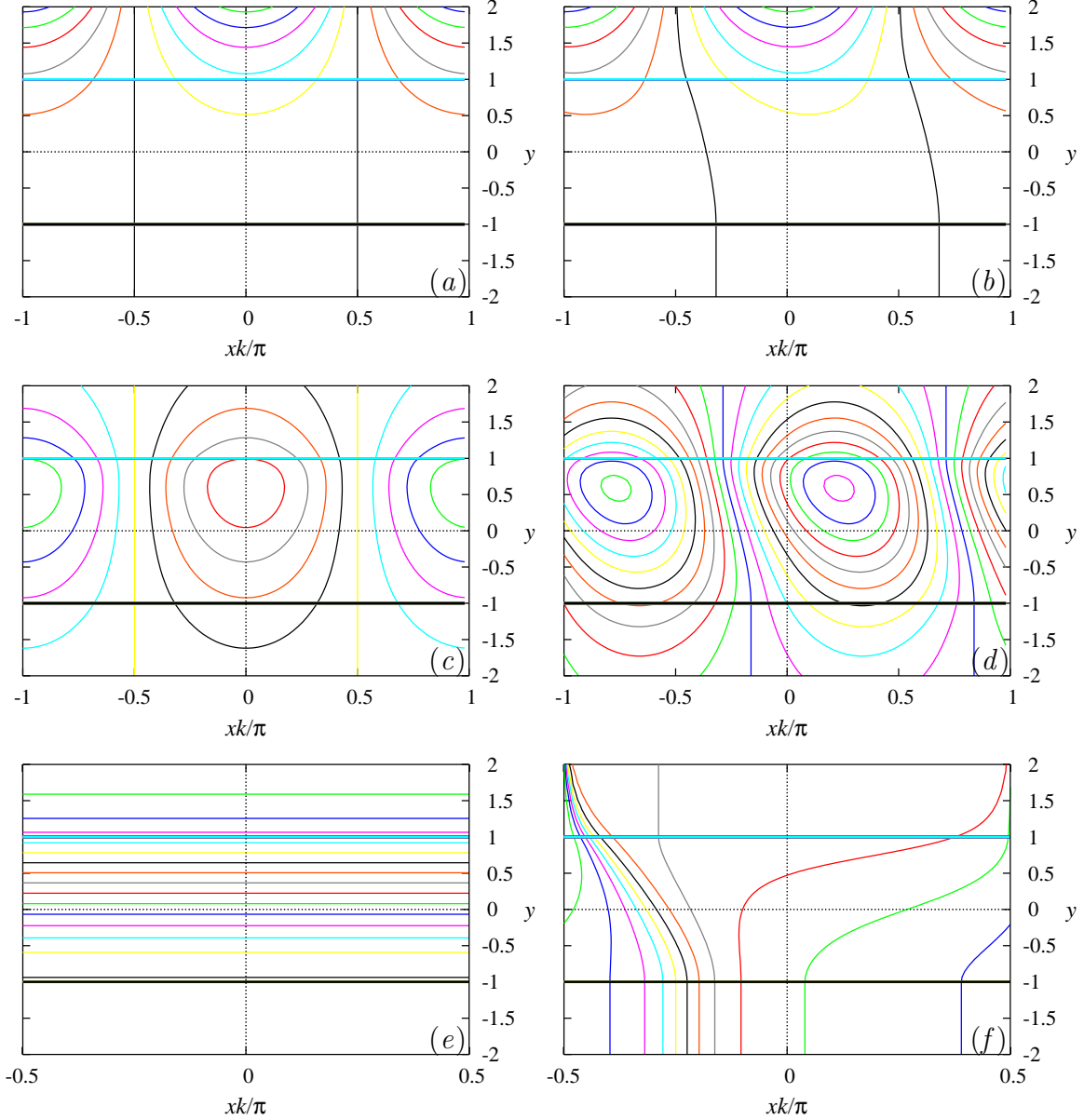


Figure 2. The magnetic flux components in the phase with the applied field (a,b), shifted by $\pi/2$ (c,d), and the corresponding phase distribution (e,f) for $\bar{\omega} = 1$ and $k = 1$ at $Rm = 0$ (layer at rest) (a,c,e) and $Rm = 1$ (b,d,f).

Figure 3(a) shows the phase distribution along the bottom of the layer over a half-wavelength between two nodes of the applied field for various dimensionless velocities Rm . Henceforth the phase φ is presented in radians and scaled by π so that $\pm\pi$ phase corresponds to $\varphi = \pm 1$. The original phase discontinuity between adjacent half-waves shows up in 3(a) as soon as the layer starts to move. The increase in the velocity is seen to smooth out this discontinuity and to shift it further downstream. Note that the total phase variation over a half-wave remains ± 1 ($\pm\pi$) regardless of the velocity, as it should be for a spatially-periodic solution.

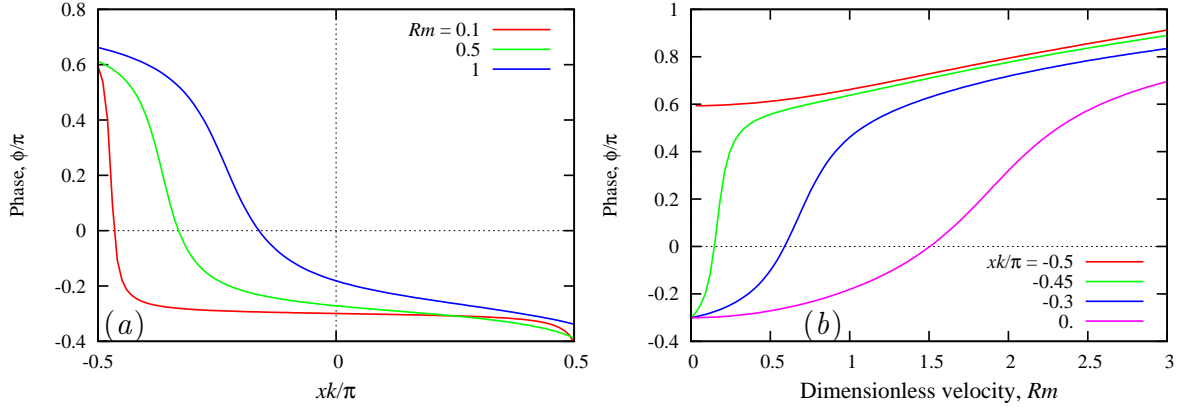


Figure 3. Phase distribution over a half-wavelength of the applied magnetic field at various dimensionless velocities defined by Rm (a) and the phase variation with Rm at different points along the bottom of the layer for $\bar{\omega} = 1$ and $k = 1$.

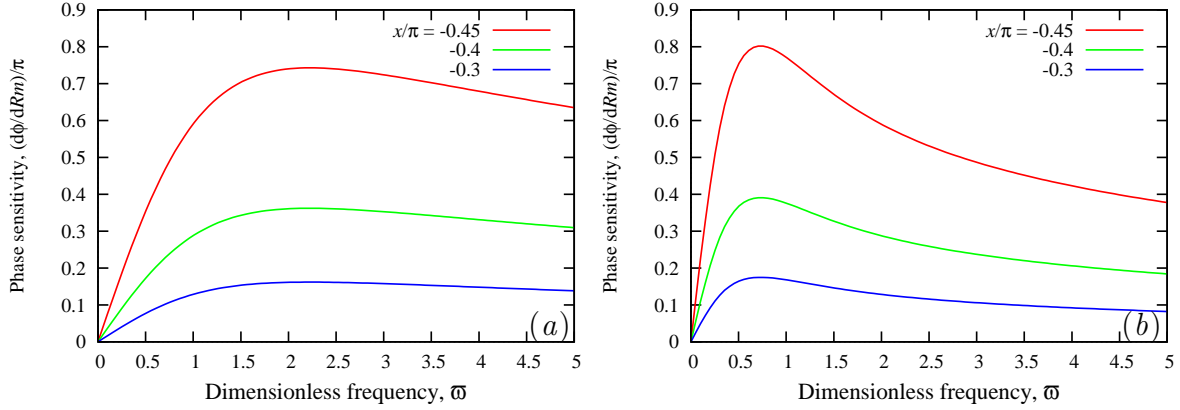


Figure 4. The phase sensitivity versus the dimensionless frequency $\bar{\omega}$ at various horizontal observation positions below the layer for $k = 1$ (a) and $k = 0.5$ (b).

The phase variation with the velocity at several observation points along the bottom of the layer is plotted in figure 3(b). As seen, the closer the observation point to the node, the steeper the phase variation, but the shorter the velocity range of this variation. The steep part of the phase variation with the velocity is obviously due to the observation point lying in the transition region between two adjacent half-waves discussed above. The phase variation is relatively weak when the observation point is located either before or after the transition region. This illustrates the importance of the location of observation point, which for low velocities should be placed downstream in close vicinity to the node or symmetry plane of the applied magnetic field, where the phase varies significantly with the velocity. In the case of the phase difference measured between two coils, the measurement sensitivity can be increased by a horizontal offset of the sensing coils with respect to the exciting coil so that one of the sensing coils gets close to the midplane, as demonstrated experimentally in the following.

To determine the optimal frequency of the applied ac field, it is useful to consider

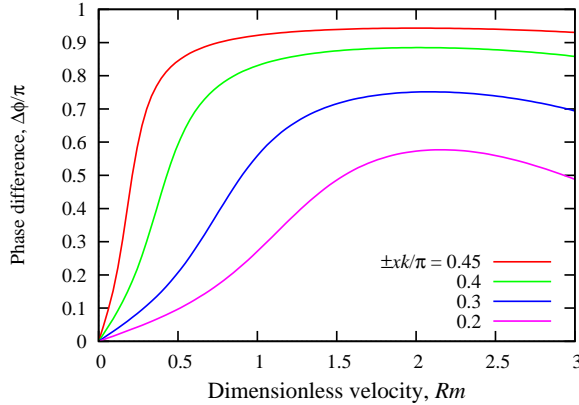


Figure 5. Phase difference between two observation points placed symmetrically with respect to $x = 0$ below the layer versus the dimensionless velocity Rm for $\bar{\omega} = 2$ and $k = 1$.

the rate of variation of phase φ with the velocity Rm . For sufficiently small Rm , which present the main interest here, the phase sensitivity is defined as

$$K = \frac{1}{\pi} \left. \frac{\partial \varphi}{\partial Rm} \right|_{Rm=0}. \quad (21)$$

This quantity plotted in figure 4 versus the dimensionless frequency $\bar{\omega}$ shows that there is an optimal ac frequency $\bar{\omega}_o$ at which the sensitivity attains a maximum. The optimal frequency, which is seen to be independent of the horizontal position of the observation point along the bottom of the layer, decreases with the wavenumber of the applied magnetic field: $\bar{\omega}_o \approx 2.1$ for $k = 1$ and $\bar{\omega}_o \approx 0.73$ for $k = 0.5$.

The phase difference between two observation points placed symmetrically at various distances from $x = 0$ below the layer is plotted in figure 5 versus Rm for $\bar{\omega} = 2$ and $k = 1$. As discussed above, the velocity sensitivity of this phase difference is seen to increase as the observation points are moved closer to the nodes at $x = \pm 0.5$. The closer the observation points to the node, the higher the sensitivity but the shorter the velocity range that can be measured. This is because the phase difference is seen first to saturate and then to reduce due to smoothing by the motion of medium. This smoothing effect limits the maximum velocity that can be measured and becomes significant at $Rm \gtrsim 2$, which corresponds to rather high physical velocities.

2.4.2. Sending coil modelled by two straight wires In this section, we turn to a more complicated external magnetic field generated by a couple of parallel wires with opposite currents separated by the horizontal distance $2s = 2$ and put at the height $h = 1$ above the layer, as shown in figure 1(b). The flux lines and the corresponding phase distribution of the vector potential are plotted in figure 6 for the layer at rest (*a,c,e*) and moving to the right with $Rm = 1$ (*b,d,f*). In the former case, the vector potential distribution is exactly anti-symmetric with respect to the symmetry plane at $x = 0$, which thus is analogous to a node in a standing wave. Correspondingly, there is a phase

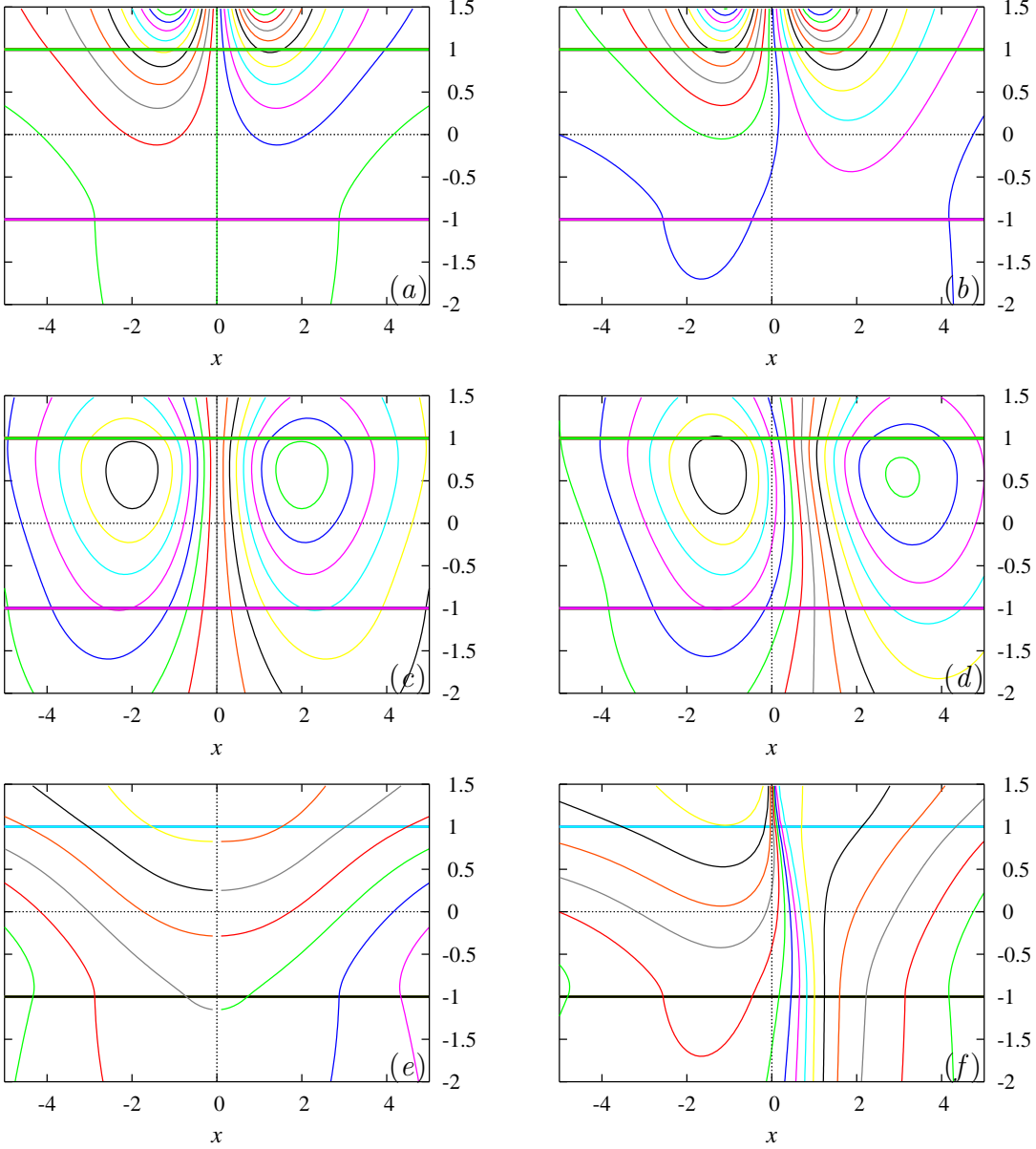


Figure 6. The flux components in the phase with the applied field (a,b), shifted by $\pi/2$ (c,d), and the corresponding phase distribution (e,f) for the external magnetic field generated by two parallel wires with $\bar{\omega} = 1$ at $Rm = 0$ (layer at rest) (a,c,e) and $Rm = 1$ (b,d,f).

jump of π at $x = 0$ when the layer is at rest. Figures 6(b,d,f) show that the motion of the layer brakes the symmetry and smooths out the phase discontinuity. Although, as seen in 6(f), the phase distribution below the layer is no more vertically invariant as for the spatially-harmonic external magnetic field considered in the previous section, its vertical variation is still weak in comparison to that of the amplitude.

Figures 7(a) and (b) show phase distributions at various velocities (Rm), and the phase variation with Rm at different points along the bottom of the layer for $\bar{\omega} = 1$. In contrast to the spatially-harmonic external magnetic field, now the phase distribution

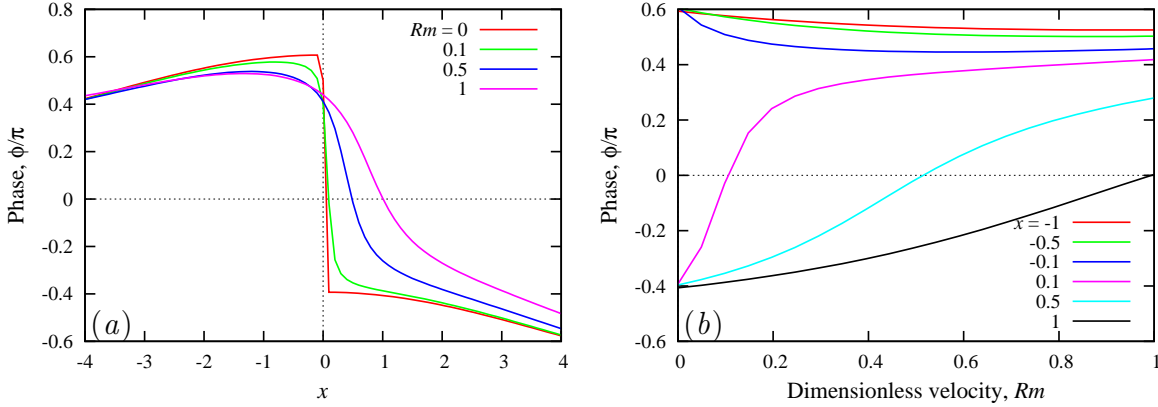


Figure 7. Phase distribution of the vector potential at various velocities defined by Rm (a) and phase variation with the velocity at different points along the bottom of the layer for $\bar{\omega} = 1$ (b).

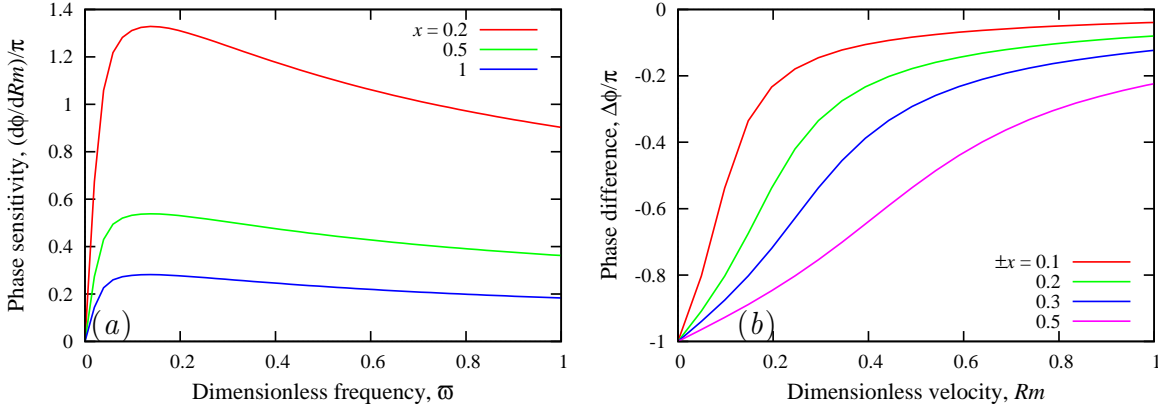


Figure 8. The phase sensitivity versus the frequency at various horizontal observation points at the bottom of the layer (a) and the phase difference between two observation points placed symmetrically with respect to $x = 0$ at the bottom of the layer versus the dimensionless velocity Rm for $\bar{\omega} = 1$ (b).

is slightly non-uniform rather than piece-wise constant along the layer even without the motion. Nevertheless, the field distribution is still symmetric with respect to the midplane between the wires. Motion is seen to break this symmetry and to smooth out the phase jump. The phase variation with velocity is shown in figure 7(b) at several points along the bottom of the layer for $\bar{\omega} = 1$. It is important to note that sufficiently close to the symmetry plane, the original phase non-uniformity at $Rm = 0$ is small relative to that induced by the motion.

The phase sensitivity introduced in the previous section, which is plotted in figure 8(a) versus the dimensionless frequency, shows that the optimal frequency at which the phase sensitivity attains a maximum for this model is $\bar{\omega} \approx 0.14$. This frequency is relatively low because in accordance to (20) the applied magnetic field is dominated by low-wavenumber (long-wave) modes. The reduction of the sensitivity above the optimal frequency is rather slow in comparison to its steep increase at sub-optimal

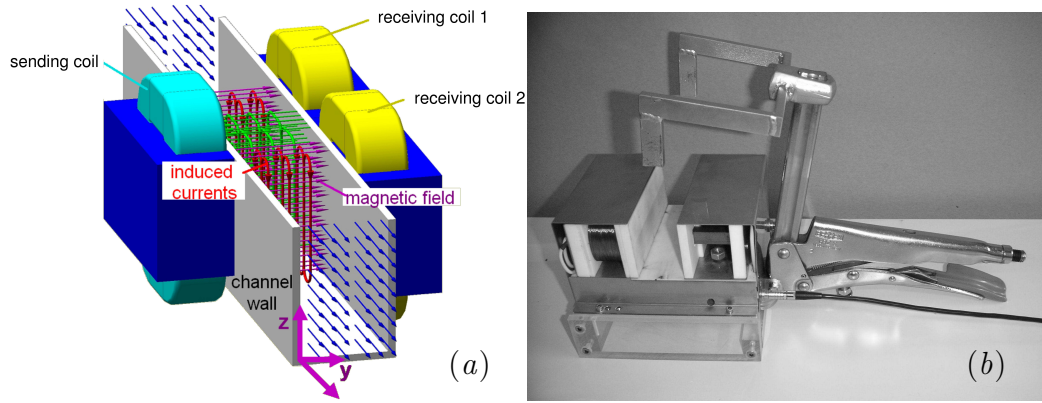


Figure 9. Experimental concept (a) and a laboratory model (b) of the phase-shift flowmeter.

frequencies. Thus, the loss of the sensitivity at $\bar{\omega} \approx 1$ is not very significant, especially for the observation points further away from the midplane. The phase difference between the pairs of observation points placed symmetrically relative to the midplane, which is plotted in figure 8(b) for $\bar{\omega} = 1$, shows the same tendency as for the spatially harmonic external field. Namely, the closer the observation points to the midpoint, the higher the sensitivity, but the faster the saturation of the phase difference. Thus, the choice of the observation points depends on the range of velocities to be measured. In this case, when the observation points are placed exactly symmetrically with respect to the midpoint, the original phase difference at $Rm = 0$ is π . This difference reduces and tends to zero with the increase of Rm as the phase is smoothed out by the advection of the magnetic field.

3. Flowmeter realization and test results

A realization of the phase-shift flowmeter based on the principles described above is shown in figure 9. It consists of two receiving coils and a sending coil, which generates an ac magnetic field, placed on the opposite sides of the duct with a liquid metal flow. This flowmeter operates like a split transformer with two secondary coils [18, 19]. The phase shift between the voltages induced in the two receiving coils is measured using a lock-in amplifier with the internal averaging time of 100 ms and the accuracy of at least 2%.

Receiving and sending coils can be placed either directly against each other or shifted by some offset l^* , as shown in figure 10. Further we refer to these two arrangements as symmetric and asymmetric ones. The theoretical analysis above suggests that such an offset may enhance the sensitivity of the flowmeter.

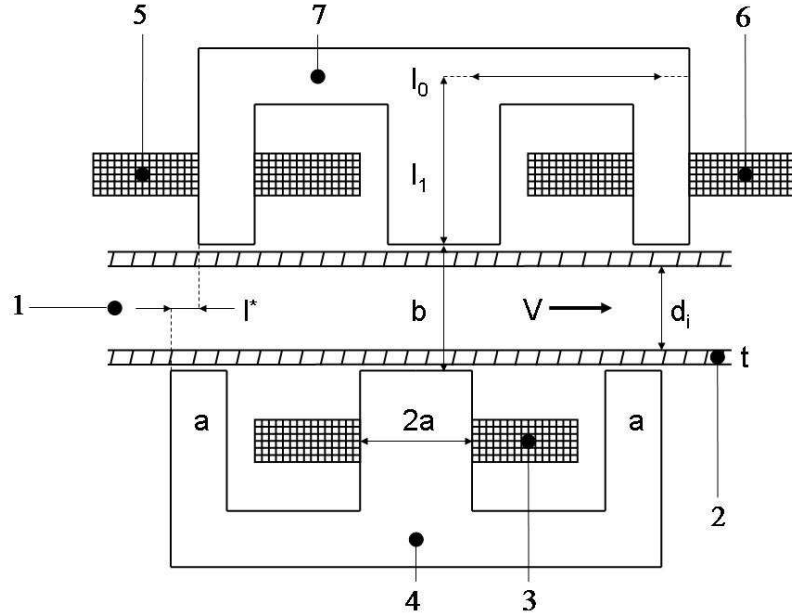


Figure 10. The flowmeter setup with a liquid metal flow of averaged velocity V in pipe (2) of diameter d_i , sending coil (3), laminated soft-iron yoke (4,7), receiving coils (5, 6), and the horizontal offset l^* between the receiving and sending coils, which is zero for a symmetric but non-zero for asymmetric arrangements.

3.1. Test facilities

The first facility is designed to operate with the eutectic melt of GaInSn, which is liquid at room temperature and has the kinematic viscosity $\nu = 3.5 \times 10^{-7} \text{ m/s}^2$ and electrical conductivity $\sigma = 3.3 \times 10^6 \text{ S/m}$ [23]. Note that a temperature increase by 1° would cause the electrical conductivity to drop by about 0.3%, which according to (5) would have the same effect as a corresponding reduction in the flow velocity. The melt is driven by a permanent magnet induction pump [20] with an adjustable flow rate. The lower part of the loop consists of circular stainless steel tubes with inner diameter of $D = 27 \text{ mm}$ and a wall thickness of 2.6 mm. The upper part consists of three independent test sections with the length of 400 mm each—all with the same inner diameter and wall thickness. These test sections can be opened and closed independently of each other by valves. During experiments, two test sections were closed, which ensured the cross-section-averaged flow velocity up to $V = 1.4 \text{ m/s}$ in the third test section. This maximum velocity corresponds to $Rm = 0.08$ with the pipe radius taken for the length scale H . The corresponding conventional Reynolds number $Re = VD/\nu \approx 10^5$ implies a strongly turbulent flow. All test sections were kept completely filled with the melt. The flow rate was independently controlled by a commercial contact-type electromagnetic flowmeter (ABB, COPA-XL25) with 0.5% accuracy, whose operation was additionally verified by local Ultrasonic Doppler Velocimetry measurements [21]. The commercial flowmeter was also used to maintain a fixed flow rate by automatically controlling the pump to

compensate for the drop in the electrical conductivity of the melt due to its ohmic heating by the pump.

The phase-shift flowmeter was attached to the tube of the GaInSn loop by a stainless steel clamp seen in figure 9(b), which allowed an easy installation on the tubes with a diameter up to 34 mm. The clamp arms were rounded in order to centre the tube in the measurement gap of the flowmeter.

Additional experiments were carried out on a sodium loop [22]. Pipes and ducts were made of stainless steel ($\sigma_w = 1.3 \times 10^6 \text{ S/m}$) with the cross-sections of 45×45 and $45 \times 40 \text{ mm}^2$ (engineering tolerance $\pm 0.2 \text{ mm}$) in the horizontal and vertical test sections, respectively, which could be separated from each other by valves. In order to avoid vibrations, in this case the flowmeter was fixed on a separate frame rather than attached to the pipe. At the operation temperature of 170°C , whose variation was negligible during the measurements, the kinematic viscosity and electrical conductivity of sodium were $\nu = 5.5 \times 10^{-7} \text{ m/s}^2$ and $\sigma = 8.3 \times 10^6 \text{ S/m}$ [23]. In this case, an increase in temperature by 1° would cause the electrical conductivity and, thus, the apparent flow rate to drop by about 0.4%. The flow was driven by an electromagnetic linear pump capable to produce the flow rate up to $31/\text{s}$, which was equivalent to the cross-section-averaged velocity of $V = 1.5 \text{ m/s}$ in the duct. This maximum velocity corresponds to $Rm = 0.35$ with the duct half-width $H = 22.5 \text{ mm}$ taken as the length scale. The corresponding Reynolds number $Re = 2VH/\nu \approx 1.2 \times 10^5$ again implies the flow to be a strongly turbulent.

Both facilities were equipped with calibrated Faraday-type electromagnetic flowmeters. These reference flowmeters were used to calibrate and test our phase-shift flowmeter, which needs to be re-calibrated when applied to another flow configuration.

3.2. Flow-rate measurements

3.2.1. Flow-rate measurements on the GaInSn loop Figure 11 shows the phase shift measured on the GaInSn loop depending on the cross-section-averaged velocity V in a pipe with insulating walls. For the emitter frequencies of 600 Hz and 400 Hz , the phase shift is seen to vary nearly linearly with the flow rate. The respective asymptotic standard errors in the best linear fits are 0.3% and 0.7%. The corresponding phase sensitivities K , defined by (21), are 0.11 and 0.095. For the harmonic wave model, figure 4 shows that these sensitivities correspond to the observation point placed at $x/\pi \approx -0.25$, i.e. about an eighth of the wavelength downstream from the node. For the emitter coil made of two straight wires according to figure 8(a), the observation point has been located at $x > 1$, which is more than a half-distance between the wires downstream from the midplane. Note that one cannot expect a quantitative agreement with these very simple theoretical models, which are supposed to capture only the basic effects but not particular details of the experiment.

To determine the frequency yielding the highest signal in the symmetric and asymmetric flowmeter arrangements, the frequency response of the flowmeter was

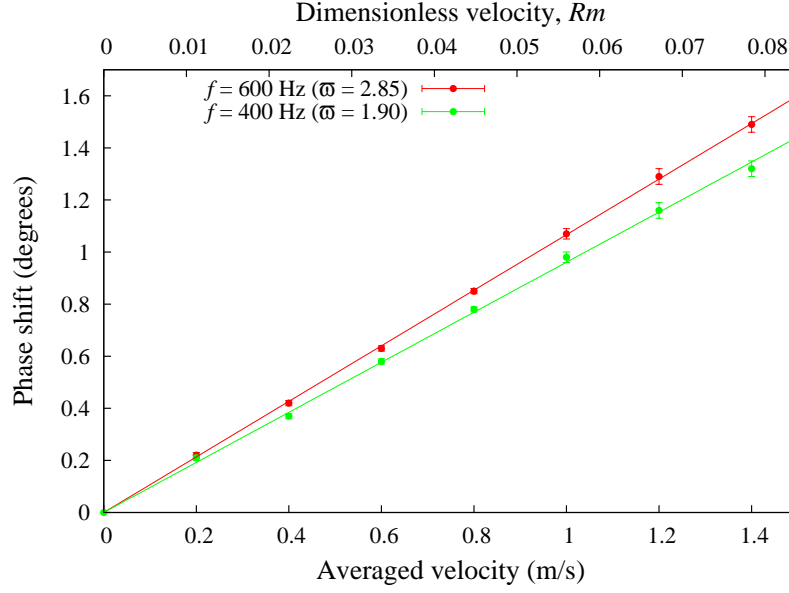


Figure 11. The phase shift measured on the GaInSn loop versus the flow-rate-averaged velocity in the symmetrically adjusted case for 600 Hz and 400 Hz emitter frequencies, which correspond to $\bar{\omega} = 2.85$ and $\bar{\omega} = 1.90$ dimensionless frequencies when the radius of the pipe $R = 13.5$ mm is used as the length scale. The measured points are fitted with straight lines crossing the origin.

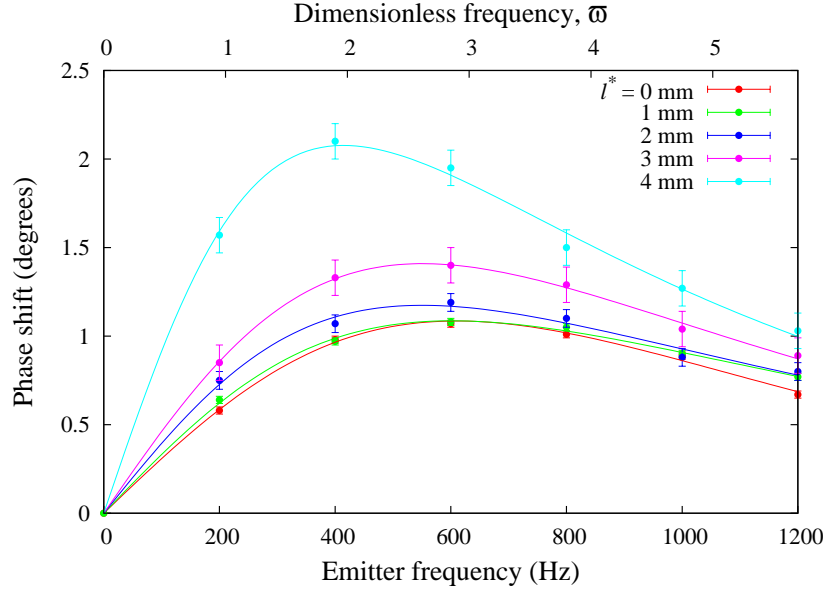


Figure 12. Frequency response measured on the GaInSn loop with insulating pipe walls for different receiving coil offsets at the averaged flow velocity of 1 m/s.

investigated (see figure 12). All experiments were carried out under the same temperature, flow rate and velocity profile of the melt. For the symmetric arrangement, the optimal frequency was about 620 Hz, which corresponds to $\bar{\omega} = 2.9$. The optimal frequency decreased to about 400 Hz when the offset was increased to $l^* = 4$ mm.

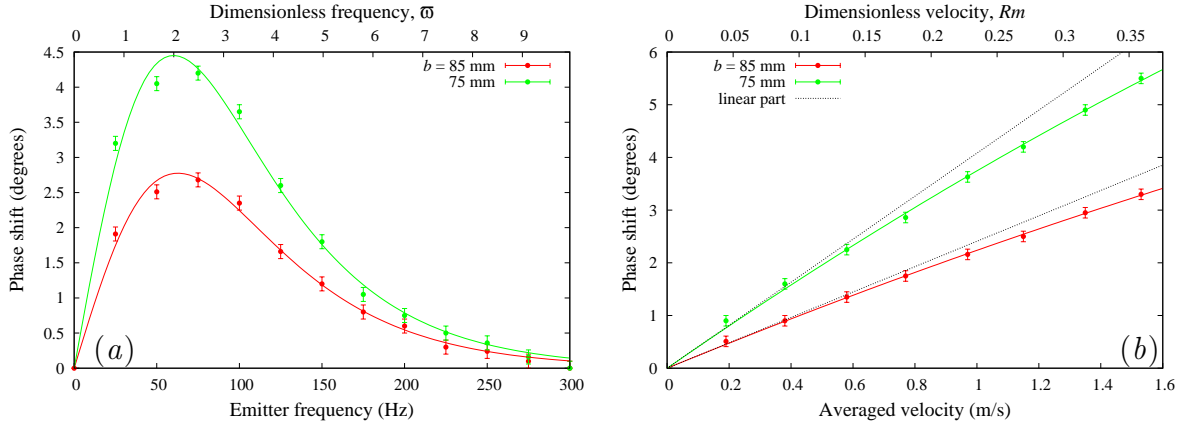


Figure 13. Measurements taken on the sodium loop with a symmetric flowmeter arrangement for the coil gaps of 85 mm and 75 mm: (a) the frequency response at the averaged velocity of 1.15 m/s ($Rm = 0.26$) and (b) the phase shift versus the averaged velocity at the emitter frequency of 75 Hz. The latter is fitted with a quadratic zero-crossing function and shown together with its linear part.

3.2.2. Measurements on the sodium loop The flowmeter used had a sending coil of 500 windings placed on the one side of the duct and two receiving coils with 1000 windings each placed on the other side of the duct. The sending coil was fed by an alternating current in the range from a few tenths up to 3 A. Both the sending and receiving coils were furnished with a high-permeability laminated yoke. The coil wires were coated with two layers of high temperature resistant polyamide ($T = 260^\circ\text{C}$). Furthermore, the coils were encased in the ceramic material MACOR, which can withstand temperatures up to 800°C and, thus, protect the sending and receiving coils from the hot pipe.

Figure 13(a) presents the phase shift measured at a fixed flow rate depending on the emitter frequency for two different widths of the gap between the sending and receiving the coils in a symmetric arrangement (see figure 10). These results show the optimal frequency of about 70 Hz, which is much lower compared to the GaInSn case due to the higher electrical conductivity and the larger duct width. This optimal frequency corresponds to $\bar{\omega} = 2.5$. The phase-shift measurements presented in figure 13(b) for two different widths of the coil gap show a noticeable deviation from the linearity, which develops with the increase of the velocity as the magnetic Reynolds number approaches $O(1)$. With the reduction of the gap with from 85 to 75 mm, the phase sensitivity (21) raises from $K = 0.057$ to $K = 0.097$, where the latter is close to the value of K corresponding to the measurements on the InGaSn loop shown in figure 11.

4. Summary and conclusions

In this paper, we have presented a conceptual design of a new contactless ac induction flowmeter for liquid metal flows based on the phase shift measurements. This flowmeter employs the fact that the flow of a conducting liquid disturbs not only the amplitude but also the phase distribution of an applied ac magnetic field. In order to figure

out the basic physical effects, we considered a simple model where the liquid flow was approximated by a solid-body motion, and the conducting medium was restricted to a layer of finite thickness. The sender coil was approximated by a spatially-harmonic standing magnetic wave in one case and by a couple of straight wires placed above the layer in another case.

In the case of an exciting magnetic field in the form of a standing harmonic wave and no flow, the phase has a typical piece-wise constant distribution along the layer with discontinuities at the wave nodes. These discontinuities are smoothed out as soon as the flow sets in and a strong phase gradient appears in the vicinity of the original wave nodes. This phase variation can be measured to determine the flow velocity. The closer the observation point to the node, the higher the sensitivity of the phase to the velocity but the lower the velocity at which the phase variation saturates. Thus, the higher the sensitivity, the lower the maximal velocity, which can be measured. There is an optimal ac frequency of the applied magnetic field which ensures maximal sensitivity of the phase with respect to the velocity at small Rm . For the observation points below the layer, the optimal frequency reduces with the increase of the wavelength of the applied magnetic field. In the case of a spatially-harmonic standing magnetic wave, the phase is independent of the vertical distance below the layer.

The phase distribution becomes more complicated when the magnetic field is generated by a coil of finite size, which was modelled by a couple of straight wires placed parallel to a conducting layer of finite thickness. In this case, the phase is no longer uniform along the layer even without the motion. However, there is still a characteristic phase jump by 180° at the midplane between the wires, while the field itself is symmetric relative to this plane. The motion of the layer smooths out this discontinuity and breaks the symmetry of the phase distribution relative to the midplane. The asymmetry of the phase distribution caused by the motion can be used to determine the velocity. For this purpose, we consider the phase difference between two observation points (receiver coils) placed symmetrically relative to the midplane. The original phase non-uniformity at $Rm = 0$ becomes relatively small when the observation points are placed sufficiently close to the midplane, which is necessary for the detection of low velocities. At higher velocities, the original phase non-uniformity becomes negligible relative to that induced by the flow. Although the optimal dimensionless frequency is rather low ($\bar{\omega} \approx 0.14$) for such a coil of finite size, where the exciting magnetic field is dominated by long-wavelength modes, the decrease of sensitivity with the frequency is slow. This allows one to work at frequencies above the optimum at $\bar{\omega} \approx 1$ without a significant loss of sensitivity. The optimal distance of observation points (receiving coils) from the symmetry plane depends on the velocity range to be measured. A smaller distance ensures a higher sensitivity, which is advantageous for lower velocities, but results in a reduced sensitivity at higher velocities because of the saturation effect.

Based on these ideas a laboratory model of such a flowmeter was built and tested on both GaInSn and sodium loops. A nearly linear relation between the phase-shift and the flow rate was measured on the GaInSn loop for the velocities up to 1.4 m/s, which

corresponded to small magnetic Reynolds numbers $Rm \lesssim 0.1$. A noticeable deviation from the linearity was observed to develop with the increase of the velocity on the sodium loop up to $Rm \approx 0.35$. The phase-shift flowmeter was found to be a robust and accurate measurement device. However, similar to standard eddy-current flowmeters, it is still sensitive to the electrical conductivity and, thus, to the temperature of the liquid.

Acknowledgments

This work was supported by Deutsche Forschungsgemeinschaft in frame of the Sonderforschungsbereich 609, and by the European Commission under contract FI6W-CT-2004-516520 in frame of the project EUROTRANS.

References

- [1] Shercliff J A 1962 *The Theory of Electromagnetic Flow-Measurement* Cambridge University Press: Cambridge
- [2] Bevir M K 1970 The theory of induced voltage electromagnetic flowmeters *J. Fluid Mech.* **43** 577–590
- [3] Engl W L, Arch. für Elektrotechnik 54 (1972) 269–277 (in German)
- [4] Shimizu T, Takeshima N and Jimbo N 2000 A numerical study on Faraday-type electromagnetic flowmeter in liquid metal system *J. Nucl. Sc. Techn.* **37** 1038–1048
- [5] Duncombe E 1984 Some instrumental techniques for hostile environments *J. Phys. E: Instrum.* **17** 7–18
- [6] Bucenieks I 2002 Electromagnetic induction flowmeter on permanent magnets *Proceedings 5th Int. PAMIR conference on Fundamental and Applied MHD (Ramatuelle, France, September)* 103–105
- [7] Bucenieks I 2005 Modelling of rotary inductive electromagnetic flowmeter for liquid metal flow control. *Proceedings 8th Int. Symp. on Magnetic Suspension Technology (Dresden, Germany, September)* 204–208
- [8] Thess A, Votyakov E V and Kolesnikov Y 2006 Lorentz force velocimetry *Phys. Rev. Lett.* **96** 164501
- [9] Thess A, Votyakov E, Knaepen B and Zikanov O 2007 Theory of Lorentz force flowmeter *New J. Physics* **9** 299
- [10] Priede J, Buchenau D and Gerbeth G 2009 Force-free and contactless sensor for electromagnetic flowrate measurements *Magnetohydrodynamics* **45** 451–458
- [11] Priede J, Buchenau D and Gerbeth G 2010 Single-magnet rotary flowmeter for liquid metals *J. App. Phys.* (submitted) arXiv:1012.3965
- [12] Lehde H and Lang W T 1948 AC electromagnetic induction flow meter *US patent 2,435,043*
- [13] Cowley M D 1965 Flowmetering by a motion-induced magnetic field *J. Sci. Instrum.* **42** 406–409
- [14] Stefani F, Gundrum Th and Gerbeth G 2004 Contactless inductive flow tomography *Phys. Rev. E* **70** 056306
- [15] Gundrum Th, Stefani F, Gerbeth G 2006 Experimental aspects of contactless inductive flow tomography *Magnetohydrodynamics* **42** 153–160
- [16] Feng C C, Deeds W E and Dodd C V 1975 Analysis of eddy-current flowmeters *J. Appl. Physics* **46** 2935–2940
- [17] Dementev S, Barbogallo F, Groessschel F, Bucenieks I, Krysko S and Poznyaks A 2002 Preliminary LBE test of the electromagnetic flow meter for the MEGAPIE target *Magnetohydrodynamics* **38** 417–422

- [18] Priede J, Buchenau D and Gerbeth G 2006 Contactless electromagnetic induction flowmeter based on phase shift measurements *Proceedings EPM Conference (Sendai, Japan, October 23-27)* 735–740
- [19] Priede J, Gerbeth G, Buchenau D and Eckert S 2008 Verfahren und Anordnung zur kontaklosen Messung des Durchflusses elektrisch leitfähiger Medien, *German patent DE 102006018623B4*
- [20] Bucenieks I 2000 Perspectives of using rotating permanent magnets for electromagnetic induction pump design *Magnetohydrodynamics* **36** 181–187
- [21] Cramer A, Zhang C and Eckert S 2004 Local flow structures in liquid metals measured by ultrasonic Doppler velocimetry *Flow Meas. Instr.* **15** 145–153
- [22] Eckert S, Gerbeth G and Lielaisis O 2000 The behaviour of gas bubbles in a turbulent liquid metal magnetohydrodynamic flow *Int. J. Multiphase Flow* **26** 45–66
- [23] Müller U, Bühler L 2001 *Magnetofluidynamics in Channels and Containers*, Appendix A.1, Springer